

Origin of Submarine Channel North of Hanish Sill, Red Sea

Neil C. Mitchell and Sarantis S. Sofianos

Abstract

Submarine channels several kilometres wide can be found near sills between major basins but they typically lie on the sides of the sills where dense bottom waters passing between the basins form gravity currents. In the southernmost Red Sea, in contrast, an 8 km-wide and 100- to 250-m deep channel lies on the north side of Hanish Sill, in an area where the strongest bottom currents flow southward, associated with winter expulsion of dense saline Red Sea deep water. Current meter data collected 10 m or more above the seabed over the sill reveal speeds occasionally exceeding 1 m s^{-1} , which are sufficient to mobilize very coarse sand and have likely prevented deposition of finer sediments in the channel, particularly for parts of the channel affected by Red Sea Outflow Water (RSOW). However, the channel extends below 200 m depths, where Red Sea Deep Water is more sluggish (typically $<1 \text{ cm s}^{-1}$). Although the stronger currents may help to maintain the upper channel morphology, it is unclear how they would have created the channel, nor can modern currents explain the deeper parts of the channel. The channel is straight and runs parallel with the spreading rift to the north, suggesting that faults may underlie the channel, though a tectonic origin (graben) is not supported by Bouguer gravity anomalies, which reveal no underlying structure. Alternatively, the channel may have originated much earlier, from massive inflow of Indian Ocean water into the Red Sea following earlier isolation and drawdown of its level. These and other possible origins of the channel are discussed in the light of limited public data from the area.

1 Introduction

The regional bathymetry of the southernmost Red Sea (Fig. 1) reveals submarine channels emanating from Hanish Sill (the shallowest point between the Red Sea and Gulf of Aden) both northward into the Red Sea and southward toward the Perim Narrows and Gulf of Aden. The strongest bottom water flow across Hanish Sill occurs in winter, comprising Red Sea deep waters made saline and dense by evaporation in the desert climate (Maillard and Soliman 1986; Pratt et al. 1999; Smeed 2004). In winter, those waters are expelled in a bottom layer while overlying less saline Indian Ocean water enters the Red Sea in a shallow surface layer to balance the outflow and evaporation losses. During summer, a three-layer water structure can develop, with Gulf of Aden Intermediate Water intruding over the sill between outflowing surface water and RSOW. The channel continuing south of Hanish Sill is associated with a density current, which is created as the dense Red Sea deep waters enter the Gulf of Aden (Chang et al. 2008; Ilicak et al. 2008; Peters and Johns 2006), forming bottom surges over about 20% of the winter period (Bower et al. 2005). In such channels, the shear stress imposed by the flow on the bed prevents deposition of finer-grade sediments, while sediments are able to accumulate on the areas outside the channel where bottom currents are weaker, leading to aggradation there. The channel is therefore a product of gravity currents as well as constraining them. Similar channels associated with density currents have been found in the ‘downstream’ sides of sills between other major basins, such as in the Black Sea north of the Bosphorus (Parsons et al. 2010) and Atlantic west of the Strait of Gibraltar (García et al. 2008).

In contrast, the Bosphorus shelf ‘upstream’ (south) of the Sea of Marmara–Black Sea sill has a broad funnel-shaped depression narrowing toward the Bosphorus (Eriş et al. 2007; Hiscott et al. 2002). Although that morphology has been complicated by fluvial erosion and delta emplacement during and following the Last Glacial Maximum (LGM) (the

N. C. Mitchell (✉)

School of Earth and Environmental Sciences, University of Manchester, Williamson Building, Oxford Road, Manchester, M13 9PL, UK
e-mail: neil.mitchell@manchester.ac.uk

S. S. Sofianos

Department of Physics, University of Athens, University Campus Buildings Phys-5, 15784 Athens, Greece

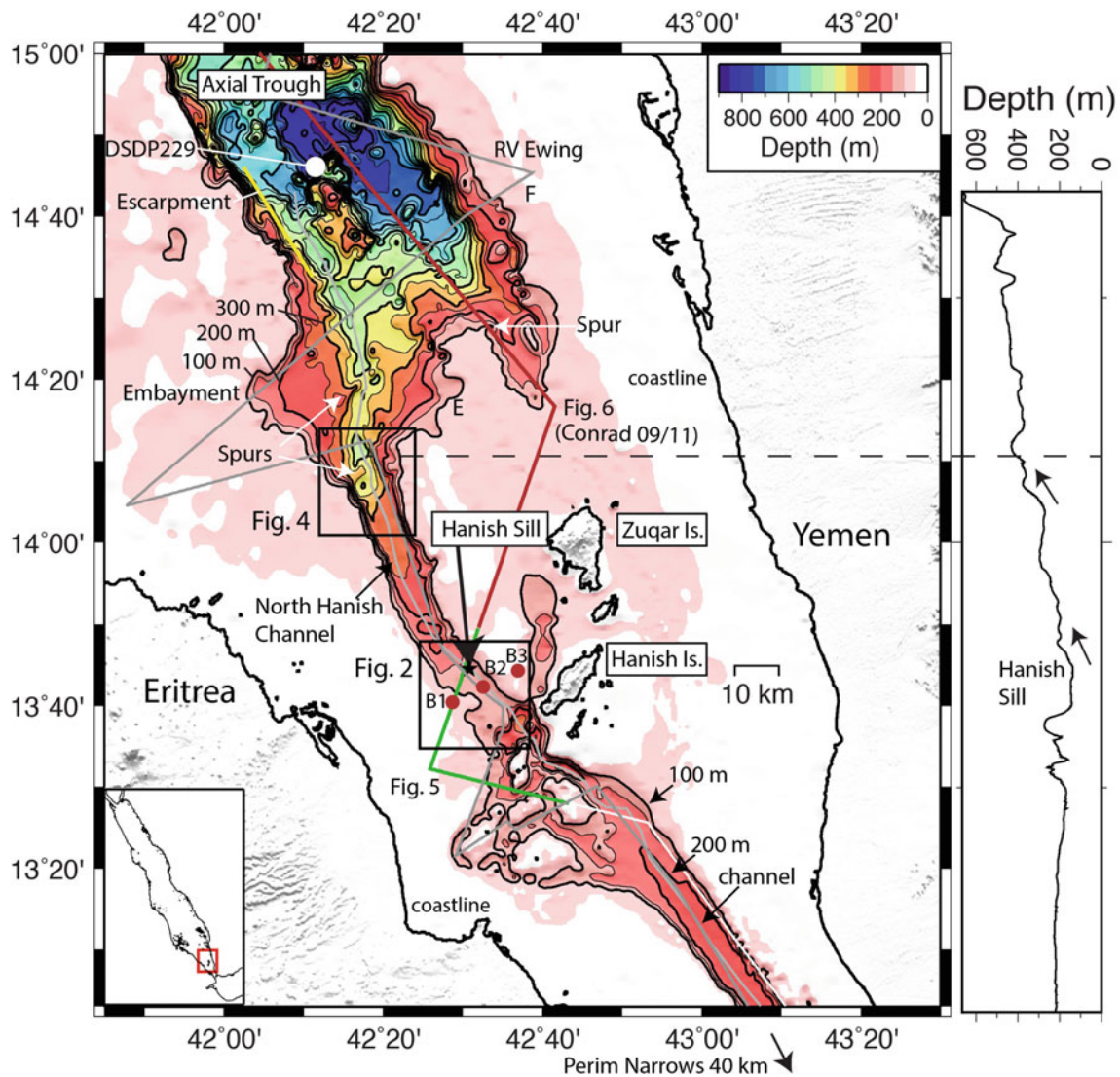


Fig. 1 Topography of the Hanish Sill area derived from the Global Multi-Resolution Topography Synthesis (Ryan et al. 2009) with color changes every 50 m (inset lower-left locates the map relative to the coastlines). Black contours are shown from 100 m to maximum depth every 50 m, with every 100 m highlighted. Black star marked “Hanish Sill” locates minimum sill depth according hydrographic charts reviewed by Lambeck et al. (2011). Solid white circle locates DSDP Site 229. White/green/red line is path of RV *Conrad* cruise rc0911 with extent of

seismic reflection data shown in Figs. 5 and 6 marked in green and dark red. Darker grey line is path of 2001 RV *Ewing* cruise (Sofianos and Johns 2007). Three solid red circles annotated B1 to B3 locate current meter stations (Sofianos et al. 2002) where the data in Fig. 3 were acquired. Annotation: E, embayment; F, line F of Sofianos and Johns (2007). Graph to right shows the depth profile of the channel (along lighter grey line in main figure) plotted versus latitude at the same distance scale as the map. Arrows mark two segments of steeper gradients discussed in the main text

shelf lies above the LGM relative sea level), the pattern of later Holocene sediment thickness (Eriş et al. 2007) does not obviously show a tendency toward developing a narrow linear channel like the north channel in Fig. 1. Additionally, no surface channel can be observed in multibeam bathymetry data collected upstream (on the east or Mediterranean side) of the Camarinal Sill (Gibraltar Strait; Luján et al. 2010). The channel north of Hanish Sill (Fig. 1) therefore seems unusual.

The data available to address the North Hanish Channel origin are unfortunately very limited. The area lies in sea-lanes and is an area of political instability, making planning of further marine data acquisition in this region problematic. Nevertheless, we make best use of the information in the limited data available to debate the different possible explanations for this channel, which we hope will help to identify areas where new data (e.g., sampling by drilling and/or seismic reflection surveys) may address this

issue more effectively in the future when better conditions prevail. We suggest that this debate is worthwhile as one of the potential origins is a massive inflow of Indian Ocean waters. If such inflow occurred, it may have been a dramatic geological event, similar to an event suggested to explain a buried channel potentially representing the Mediterranean re-flooding following the Messinian Salinity Crisis (MSC) (Garcia-Castellanos et al. 2009). As with the Mediterranean re-flooding, the event would have potential implications for how unconformities around the basin were created, how isostatic adjustment occurred as a result of water loading of the basin, how abruptly water exchanges with the Indian Ocean changed (with paleoceanographic effects) and how abruptly the regional climate changed.

2 Datasets and Methods

Current meter records were collected over an approximately 18-month period with instruments installed close to the seabed at sites B1–B3 (Figs. 1 and 2) (Sofianos et al. 2002). Data were collected at the deepest site B2 with an acoustic Doppler current profiler (ADCP) whereas conventional Aanderaa impeller meters were used at the other sites. Summaries of the data collected are shown along with information on the measurements in Fig. 3.

The bathymetry and elevation data shown in Fig. 1 are from the Global Multi-Resolution Topography Synthesis (Ryan et al. 2009), with the bathymetry constructed from track-line data (mainly passage soundings) and depths between ship tracks interpolated using the marine gravity field derived from satellite altimetry data (Sandwell and Smith 1997; Smith and Sandwell 1997). Features interpreted from this grid are constrained by numerous passage soundings of vessels passing through the Bab al Mandab Strait. The data are shown contoured every 50 m below 100 m to highlight the channel and Axial Trough morphology (for comparison, the 113-m depth level corresponds with the local water level over the sill at the time of the LGM (Lambeck et al. 2011)).

Echo-soundings were collected around the Hanish Sill in 1971 and 1972 by Werner and Lange (1975). Figure 2 shows a map constructed by digitizing the 10-m depth contours shown by Werner and Lange (1975) and interpolating using the “surface” software module (Smith and Wessel 1990). The 1971 surveys (white lines in Fig. 2b) were carried out with visual bearings to Hanish Island, whereas the 1972 survey (black lines in Fig. 2b) was aided by radar reflectors placed on two navigation buoys located in Fig. 2b. The large open circle in Fig. 2a highlights a small inner channel observable immediately north of Hanish Sill. Of the profiles shown in Fig. 2a, 5022 runs along the lip of the sill, where the shallowest point of the channel reaches 137 m depth in the Werner and Lange (1975) survey, and

5025 crosses the channel on the Red Sea side of the sill. In Fig. 2c, magnetic anomalies collected along the RV *Jean Charcot* track crossing the sill are shown projected against the vessel’s trackline.

Figure 4 shows the bathymetry of the lower part of the channel immediately before it reaches the Axial Trough. This map was obtained by gridding the available track-line sounding data from the National Geophysical Data Center (NGDC). In Fig. 4, bathymetry along four tracks are also shown in red (profiles projected perpendicular to tracks after removing an offset of 300 m).

Seismic reflection data were collected during RV *Conrad* cruise rc0911 along the line marked in Fig. 1. According to information from the NGDC, these data were collected with a 25 cubic inch airgun. Despite their age, the records shown in Figs. 5 and 6 are of sufficient quality to reveal sub-surface reflections beneath the slope NW of Hanish Sill and the area NW of Hanish Island. Their large vertical exaggeration ($\sim 15\times$) needs to be considered when attempting to interpret dips of features in the data.

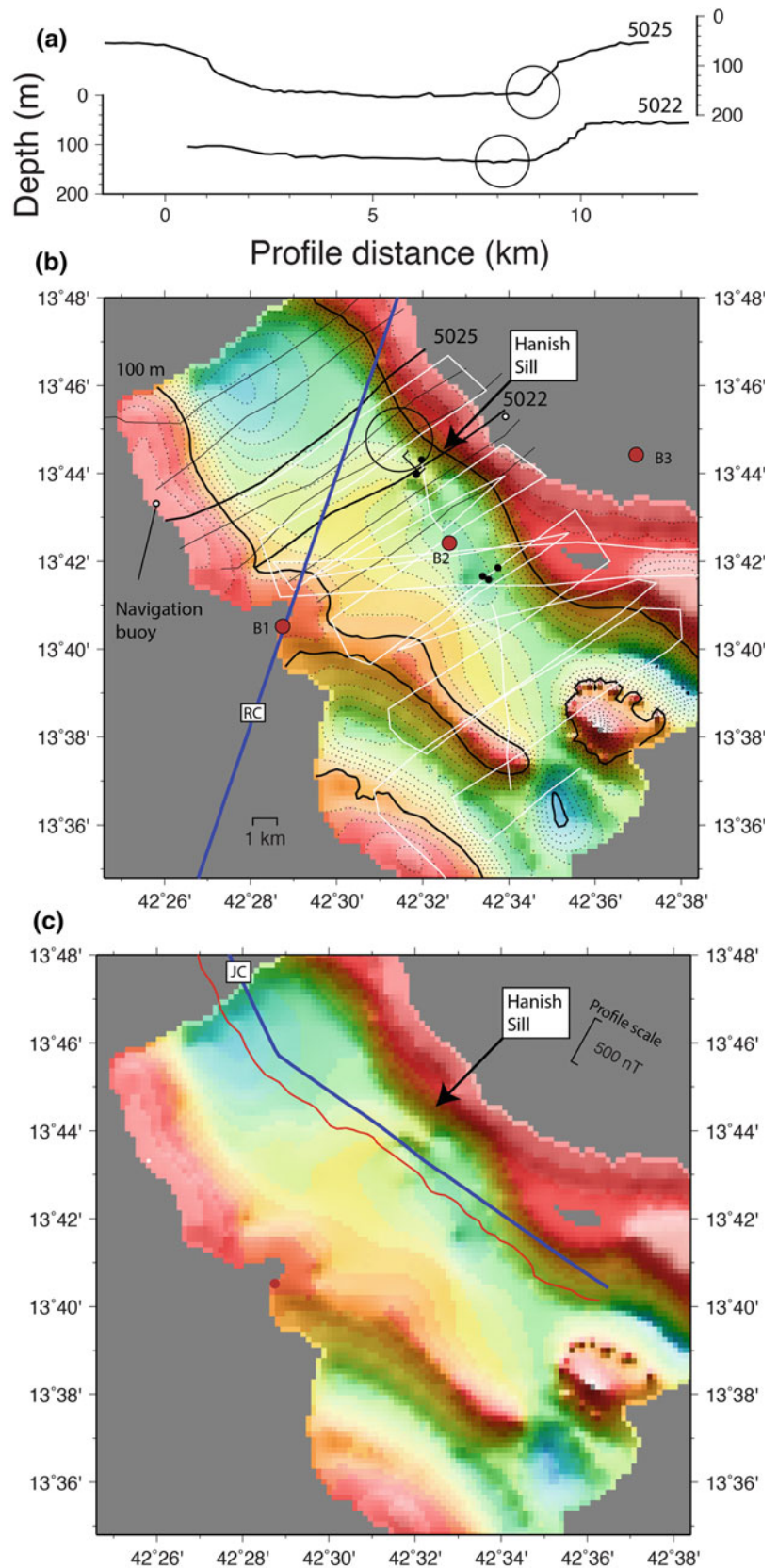
Structure beneath Hanish Sill, the channel and surrounding areas can also be assessed from gravity data. The marine free-air gravity field shown in Fig. 7a was created using data from satellite altimeters; in open ocean areas these gravity data have comparable precision to shipboard gravity data (Sandwell et al. 2014). However, a study by Mitchell (2015) comparing shipboard gravity measurements in the northern and central Red Sea with the earlier version 18 of the altimeter-based gravity field found long-wavelength mismatches of up to 10–20 mGal that are potentially artifacts of ties with terrestrial gravity measurements. Hence, gravity anomalies along the coasts, such as that along the Yemen coast in Fig. 7a, should be interpreted cautiously.

To reduce the effects on the gravity anomalies of the seabed topography, a map of Bouguer gravity anomalies was calculated and is shown in Fig. 7b. This was computed below sea level using a density contrast of $1.77\text{--}1.03\text{ g cm}^{-3}$, where 1.77 g cm^{-3} is the mean density of the upper 200 m of sediment from physical property measurements made on DSDP Site 229 samples (Manheim et al. 1974; Whitmarsh et al. 1974) (Fig. 1) and 1.03 g cm^{-3} is seawater density. Above sea level, a 2.3 g cm^{-3} density that is typical for the upper 1 km of volcanic rocks on Hawaii and in the rift zone of Iceland was used based on sources compiled by Rubin (1992).

3 Information on Seabed Sediments

Sediment grain size and density are important for inferring particle threshold of motion and for assessing how the geomorphology may have formed from sediment erosion or deposition. Unfortunately, there is very little information on the seabed sediments around the sill. Werner and Lange

Fig. 2 Bathymetry of the sill based on data of Werner and Lange (1975). **a** Two bathymetry profiles located with bold lines in **b**. Circles mark a channel in profile 5025 and the minimum elevation at the sill in 5022. **b** Map of bathymetry constructed from the 10-m depth contours in the map of Werner and Lange (1975), with 100 m contour in bold and 10 m contours dotted. Open circles: navigation buoys; closed circles: bottom sample stations; white lines: 1971 surveys; solid straight lines: 1972 survey; dark red symbols, current meter sites as Fig. 1; blue line, path of RV *Conrad* (RC). **c** Red line with scale to upper right shows residual magnetic anomalies collected along RV *Jean Charcot* track (blue line)



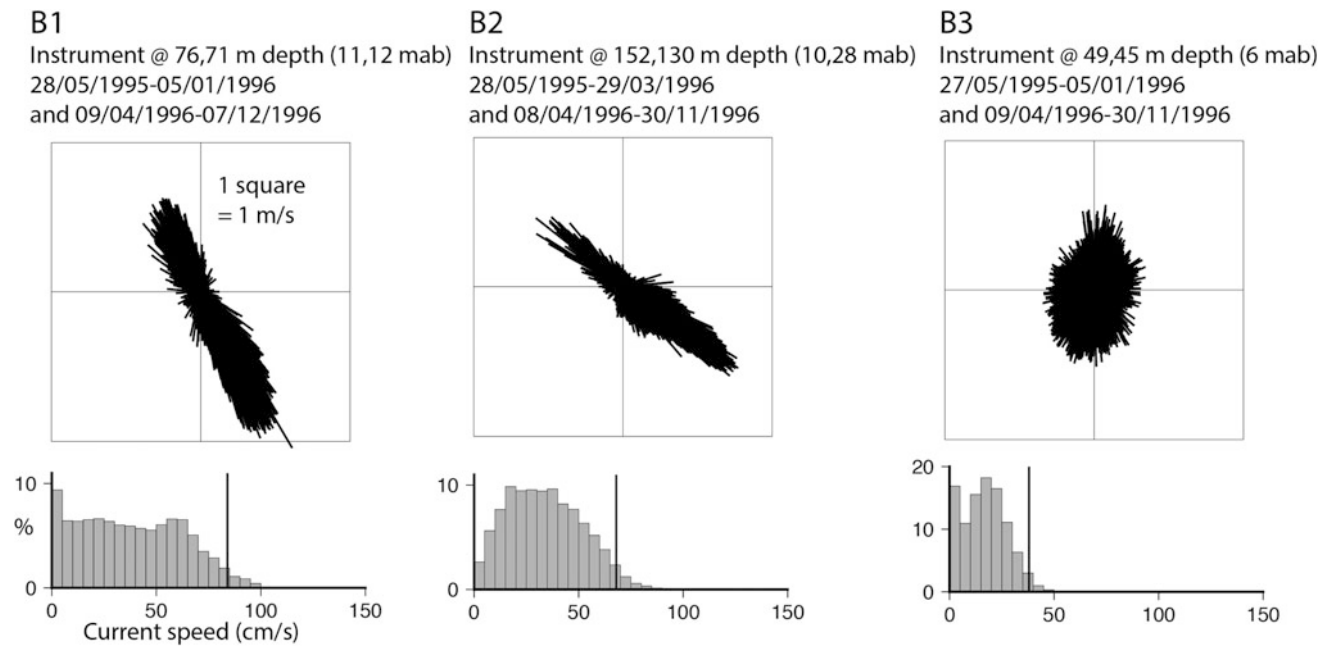
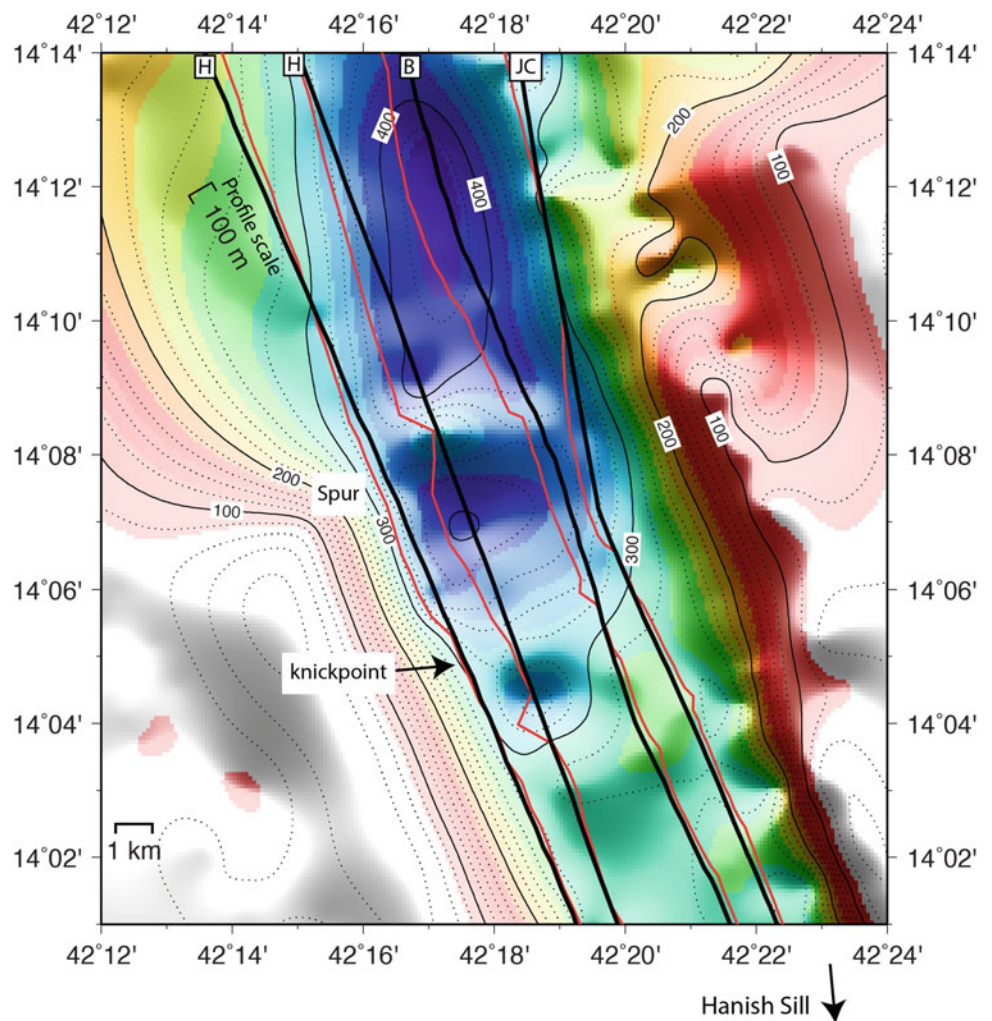


Fig. 3 Summaries of data from current meters deployed near the seabed at sites B1–B3 shown in Fig. 1 (Sofianos et al. 2002). Data in the vector plots (upper graphs) are drawn at a scale such that a distance across one square is equivalent to a current speed of 1 m s^{-1} . In the histograms of current speeds, vertical bars locate the 95-percentile of each distribution

Fig. 4 Detail of the lower channel knickpoint. Bathymetry in background was generated by gridding the available track-line data and contoured every 20 m (dotted lines) with 100 m intervals annotated (bold lines). Also shown are tracks with depth soundings plotted (red lines) toward N060°E with profile scale in lower left for (H) two passages of HMS *Herald* (1996), (B) one passage of HMS *Beagle* (1995) and (JC) one passage of RV *Jean Charcot* (1983). Depths have been offset by 300 m before projecting perpendicular to vessel tracks. (The bathymetry interpolation was carried out with the minimum curvature option of the “surface” module of the GMT software, which creates artifacts in areas lacking data (Smith and Wessel 1990), hence the hill under annotation “knickpoint” in the figure is an artifact)



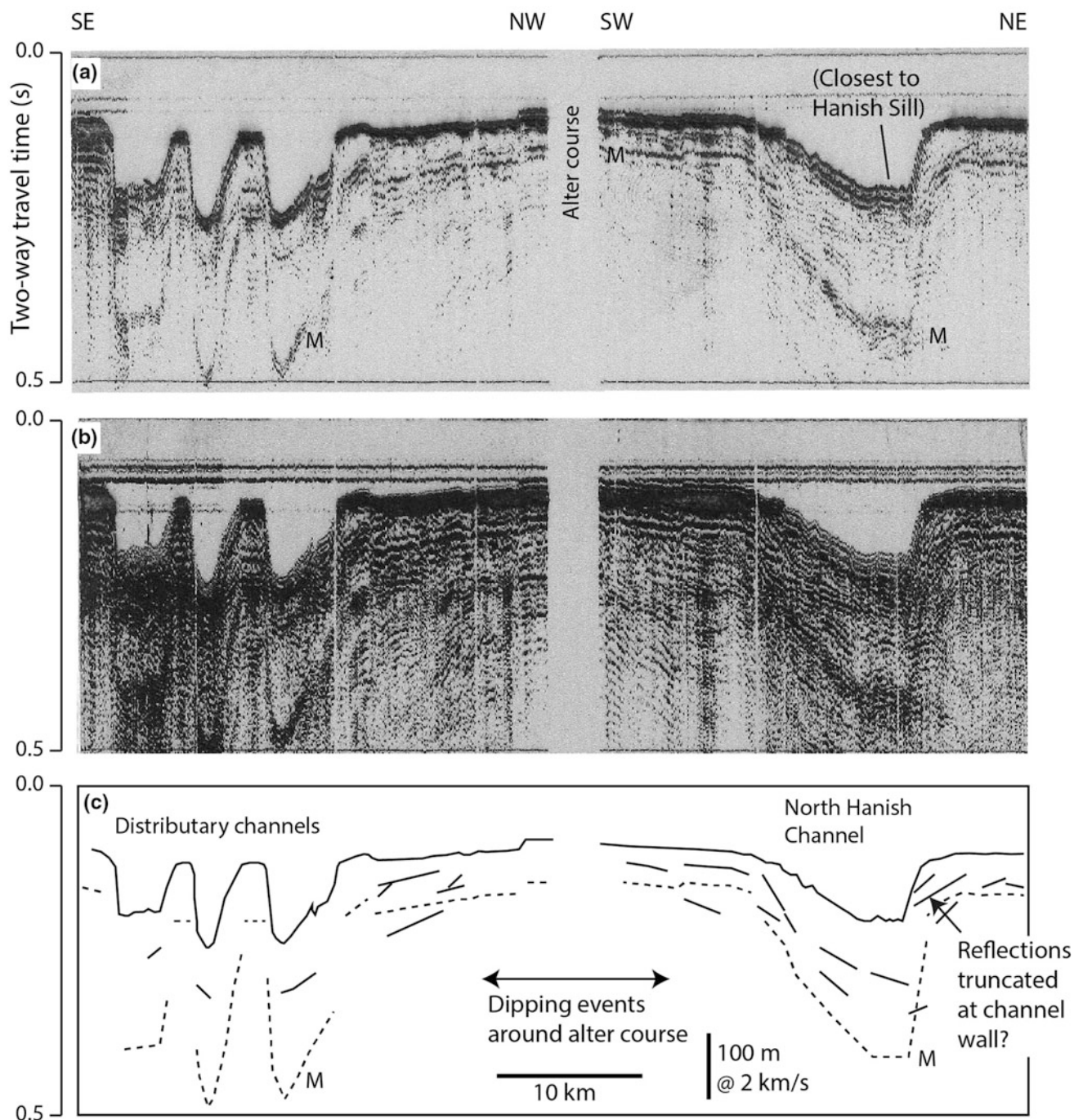


Fig. 5 Analogue seismic reflection data collected on RV *Conrad* during cruise rc0911 adjacent to Hanish Sill (along the track located by green line in Fig. 1): **a** with low-gain amplification, **b** with high-gain amplification and **c** interpretation. Black represents high reflection amplitude. Vertical exaggeration below seabed is approximately 15:1. Annotation 'M' represents water-column first multiple (dashed lines in

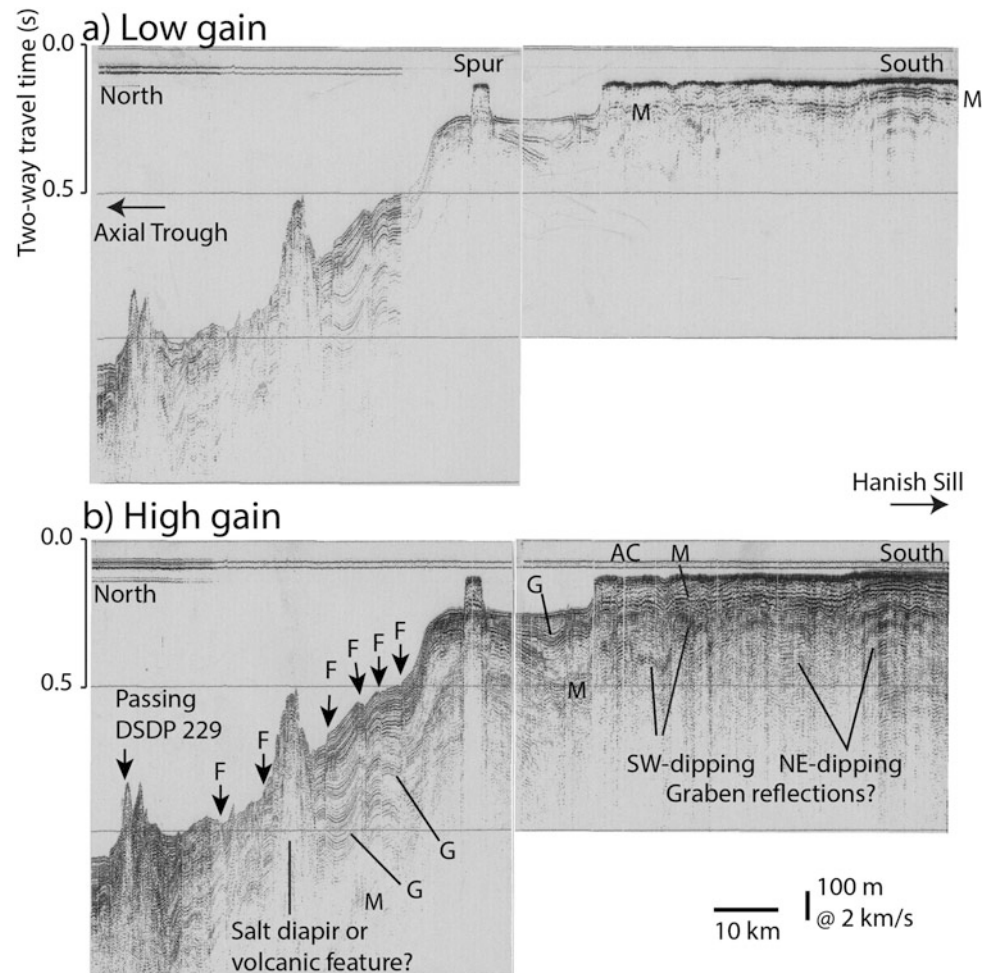
c). Multiple arrives earlier than double the seabed reflection time because of the shallow water and finite source-to-receiver offset compared with water depth (horizontal offset from airgun to acoustic centre of the streamer estimated to be ~60 m from 37 m water depth and ~91 ms two-way time at alter course position). Note also that horizontal line near 0 s TWT in **a** is not zero-time mark

(1975) mentioned finding live coral fragments in a grab sample recovered from over the sill. Cores recovered at DSDP Site 229 north of the sill (Fig. 1) were described in the drilling reports (Whitmarsh et al. 1974) as containing 212 m of clay-rich nanofossil carbonate ooze of Late

Pleistocene age (up to ~25 ka according to the GeomapApp (www.geomapapp.org) revised sediment chronology for the site).

Einsele and Werner (1972) described the textures and mineralogy of seabed sediment recovered at 12 sites south of

Fig. 6 Analogue seismic reflection data collected on RV *Conrad* during cruise rc0911 north of Hanish (located by red line in Fig. 1): **a** low-gain amplification and **b** high-gain amplification (black is high reflection amplitude), as in Fig. 5. Annotation: ‘M’, water-column first multiple; ‘F’, shallow fault; ‘G’, tectonic growth structure; ‘AC’, alter course



the sill in an area centred on the Perim Narrows. They found that the shelf and channel sediments comprise dominantly biogenic particles derived from the adjacent nearshore areas and from in situ production. On the shelf immediately north of the Perim Narrows, bryozoan fragments dominated, with lesser benthic foraminifera, coral fragments and septula. Some sampling sites within the narrows contain hardgrounds with pebbles and shell fragments. At one site further north within the Axial Trough at $\sim 14^{\circ} 50'N$, a sample was recovered containing dominantly pelagic foraminifera and gastropoda, and lesser scaphapoda and pteropoda.

Based on these studies, the particles entering the area of the channel north of Hanish Sill are likely mostly biogenic and have a wide range of grain sizes. Grain size is not conservative as biological particles can be easily broken into smaller particles during transport by currents. The authors of the report for DSDP Site 229 (Whitmarsh et al. 1974) suggested that the fine particles there had been swept from the shelves by seasonal currents. Given the dominant biogenic nature of these sediments, their bulk grain densities are likely lower than siliclastic particles such as quartz because of pore spaces commonly within them.

4 Observations

4.1 Bathymetry

4.1.1 Overview

Hanish Sill (Fig. 1) lies in the area of a southward-narrowing sea between the coasts of Arabia and Africa, though it is not at the narrowest point (which lies further south at Perim Narrows). Volcanically active islands (Hanish and Zuqar) lie east of the sill (Gass 1970). Bathymetry of the area is generally shallow, forming broad shelves of <100 m depth. This shallow bathymetry is interrupted north of $14^{\circ}20'N$ by the southernmost end of the Axial Trough, which contains the active spreading centre (Garfunkel et al. 1987). The seabed within the trough deepens below 500 m to the north in Fig. 1. South of Hanish Sill, the bathymetry contains a series of closed-contour highs, which likely formed islands during the LGM (Lambeck et al. 2011). Two major channels can be observed in Fig. 1. One runs to the SE, whereas a second (the focus of this article and referred to as “North Hanish Channel”) runs NNW of the sill, on its Red Sea side.

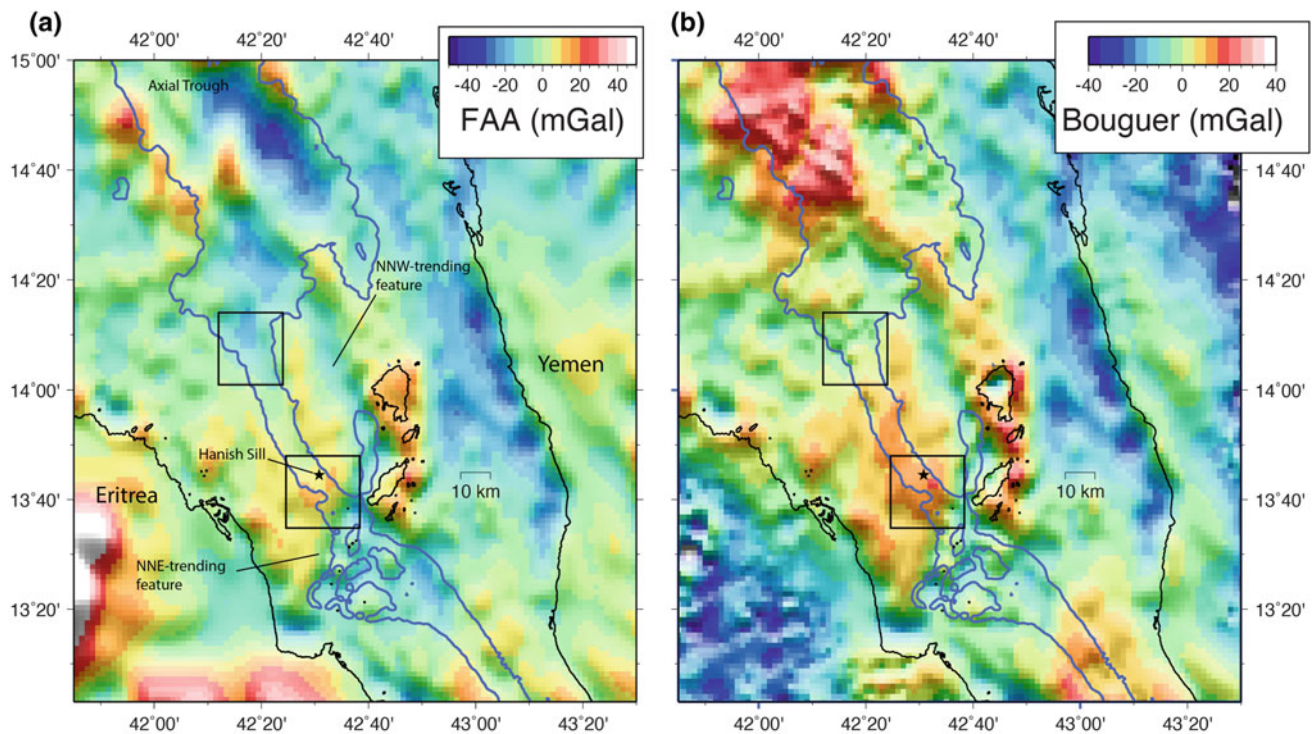


Fig. 7 **a** Free-air gravity anomalies derived from satellite altimetry (marine areas) from Sandwell et al. (2014) (their version 22). **b** Bouguer gravity anomalies derived using the gravity slab formula by correcting the free-air anomalies for a 2.3 g cm^{-3} density above sea

level and for a $(1.77\text{--}1.03 \text{ g cm}^{-3})$ seabed density contrast below sea level. Blue contour is 100 m depth level. Other annotation as Fig. 1, which covers the same area.

North Hanish Channel is 8-km wide. In cross-section, it has a vertical relief of 100–250 m and its base is mostly flat. The mean gradient from the sill to the edge of the Axial Trough is $\sim 0.9\%$ (0.5°). Steep sections of the along-channel profile (marked by arrows in the graph in the right panel of Fig. 1) occur just below the edge of the sill and about 10 km south of where the channel enters the Axial Trough. Two spurs of 50–100 m elevation extending into the channel are marked in Fig. 1.

4.1.2 Hanish Sill

In Fig. 2b, the sill lies within a broad depression, about 8 km across, on the east side of a broad NE-SW-oriented ridge crossing the depression. Immediately north of the sill, a small $\sim 10\text{-m}$ deep channel runs NW (circled in Fig. 2b). A further 3 km down the channel, profile 5025 shows a corresponding small depression (circled in Fig. 2a). Profile 5022 runs along the sill and reveals a mainly low-relief seabed, though with a small depression of perhaps a few metres (circled) where the sill minimum elevation was proposed by Werner and Lange (1975) to be located at 137 m depth. Running southeast of the site of current meter B1, a ridge of >50 m elevation causes a modest narrowing of the central depression to the SE and a closed-contour high occurs east of its tip ($13^\circ 38' \text{N}$, $42^\circ 36' \text{E}$). The *Jean Charcot*

magnetic anomalies (Fig. 2c) vary modestly with amplitudes of ~ 100 nT and rise only by 100–200 nT on crossing the sill.

4.1.3 Lower Channel

Figure 4 shows enlarged bathymetry where the channel is unusually steep ($14^\circ 04' \text{--} 14^\circ 07' \text{N}$). In river channels, such morphological features are described as “knickpoints”, so we use this term here. The four lines of passage soundings plotted as profiles (red lines) in Fig. 4 also reveal this morphology. One of the spurs mentioned earlier can be observed in the central two lines of passage soundings.

4.2 Currents

The current meter data summaries (Fig. 3) reveal the stronger outflows (to SE) for sites B1 and B2 relative to inflows, while currents at the shallower site B3 are smaller and less asymmetric. The 95-percentile current speeds (marked by vertical bars in the lower graphs of Fig. 3) are 84, 68 and 38 cm s^{-1} for B1, B2 and B3. The constriction provided by the ridge (Fig. 2b) may explain the greater speeds at B1 compared with B2, much like how headland-attached sand banks can lead to accelerated currents passing over them.

4.3 Gravity Anomalies

The free-air anomalies (Fig. 7a) reveal two gravity depressions, one running NNE just west of Hanish Island and another running NNW roughly orthogonal to the long axis of Hanish Island. These two trends also occur in the computed Bouguer anomalies (Fig. 7b), so they most likely represent underlying linear bodies of lower density than their surrounding rocks. The NNW feature forms a Bouguer anomaly trough of about 10–20 mGal. The source of the anomaly can be very roughly evaluated using the gravity slab formula (Telford et al. 1976). Thus, a 20 mGal anomaly could potentially be created by a density contrast of 1.0 g cm^{-3} between superficial sediments and a denser basement with 500 m of relief. Hanish Sill is associated with somewhat elevated Bouguer anomalies of about 15–20 mGal.

In contrast, the linear feature in the free air anomaly following the channel north of Hanish Sill does not appear in the Bouguer anomaly; the free air feature is explained simply by the effect of seabed topography. Bouguer anomalies computed using an alternative seabed density contrast of $2.0\text{--}1.03 \text{ g cm}^{-3}$, where 2.0 g cm^{-3} is a typical density of shelf sediments (Hamilton and Bachman 1982), produced a similar result.

4.4 Seismic Reflection Data

Although water-column multiples obscure some features, the seismic data reveal dipping reflections beneath the slope immediately north of Hanish Sill (SW to NE section in Fig. 5). The large vertical exaggeration of the data make these shallow dipping features appear steep; the west bank of the North Hanish Channel marked in Fig. 5c has an along-profile gradient of less than 1° . Beneath the North Hanish Channel, sub-bottom reflections all appear to dip with the same sense as the channel floor. Reflections can be observed up to 150 ms two-way travel time below the seabed reflection ($\sim 150 \text{ m}$ sub-bottom depth if the shallow sediments have 2 km s^{-1} seismic velocity). However, beneath the northeast wall of North Hanish Channel, one or two reflections dip to the southwest and appear to be truncated at the seabed (channel wall).

Further sub-surface reflections can be observed in the data beneath the distributary channels (left side of Fig. 5). Around the change of vessel course in Fig. 5, a series of reflections can be observed. They appear to dip to the SE before the course change and to the NE after the course change (dip components along the sections). These may represent strata or other layered features dipping to the east beneath the west side of Hanish Sill.

To the south in Fig. 6, some dipping reflections underlie the area of the NNW-trending Bouguer gravity anomaly

trough described earlier and thus may represent a small graben. Immediately northwest of there, the *Conrad* track ran over the southeasterly embayment of the Axial Trough (Fig. 1) and the corresponding seismic record in Fig. 6 reveals locally thickened intervals between reflections suggesting a tectonic growth structure (“G” in Fig. 6). The track then crosses a spur of elevated seabed with character in the seismic data much like those collected over the shelves.

Further northwest of there, where *Conrad* crossed the southeast submarine slope of the Axial Trough, the record reveals a series of abrupt disruptions of reflections suggesting the presence of shallow faults (“F” in Fig. 6). These faults and further growth structures most likely represent the effects of slumping of superficial sediments into the Axial Trough. The slope also contains an isolated peak without internal structure, which we speculate is a salt diapir or volcanic edifice. The seismic data collected adjacent to DSDP Site 229 reveal some seabed layering, which may represent the same hemipelagic sediments recovered at that site (Whitmarsh et al. 1974).

5 Discussion

5.1 Currents Affecting Channel Morphology

The $\sim 1 \text{ m s}^{-1}$ peak currents recorded at sites B1 and B2 are likely to prevent deposition of fine and silt grade particles and many sand grade particles. For example, a 1 m s^{-1} threshold velocity at 1 m above the bed would mobilize quartz sand up to 4 mm in diameter according to Miller et al. (1977). Threshold speeds for biogenic clasts can be smaller because of the lower net densities of porous clasts. In settling experiments, densities of foraminifera tests have been found to be 1.162 g cm^{-3} (Berthois and Le Calvez 1960) and 1.500 g cm^{-3} (Berger and Piper 1972). Their densities relative to seawater ($\sim 1.03 \text{ g cm}^{-3}$ in the Red Sea) are thus small compared with quartz. Southard et al. (1971) measured the thresholds of motion of carbonate ooze comprising mainly foraminiferal tests and coccolithophorid remains, which Miller and Komar (1977) converted to velocity at 1 m above the bed. Those values vary from only $9\text{--}13 \text{ cm s}^{-1}$ with no compaction to $\sim 20 \text{ cm s}^{-1}$ after some compaction. Thresholds of motion of larger particles are difficult to predict given the strongly varied effect of grain shape of biogenic particles (Paphitis et al. 2002). Nevertheless, threshold velocities should be lower than for quartz clasts. The 95-percentile velocities recorded at current meter sites B1, B2 and B3 imply mobilization of quartz grains up to diameters of 2, 1.4 and 0.2 mm according to the data of Miller et al. (1977), which are therefore minima. Hence, at least very coarse sand would be mobilized in the channel and fine sand would be mobilized at Site B3. These currents

maintain the geomorphology of the sill by preventing the finer sediment grades from depositing within the central depression (Fig. 2).

However, going northwest from the sill and into deeper water, bottom currents are likely to be weaker. This is partly a consequence of the funnel shape of the southernmost Red Sea. Furthermore, potential densities in the southernmost Red Sea increase with depth (e.g., Jarosz et al. 2005) and oppose any significant upward movement of deep waters. RSOW with a potential density of $\sim 1028 \text{ kg m}^{-3}$ overlies Red Sea Deep Water (RSDW) with a potential density of $\sim 1028.6 \text{ kg m}^{-3}$, with a boundary between the two at around 200 m (Sofianos and Johns 2003). Consequently, RSOW probably originates from intermediate depths in the Red Sea (Cember 1988; Neumann and McGill 1962; Sofianos and Johns 2003). Although collected in summer when the outflow is less intense, ADCP data collected along line F in Fig. 1 (Sofianos and Johns 2007) revealed negligible current speeds ($<1 \text{ cm s}^{-1}$) below 200 m. Thus, the northern part of the channel, where it lies deeper than 200 m, is likely to contain less mobile RSDW. The prevalence of slope failure features in Fig. 6 further supports this view, as such features typically form in muds (deposited under weak currents) rather than coarser grade unconsolidated clastic particles. Deposition of muds is more likely to fill in the lower channel than create its morphology.

5.2 Slope Failure Origin

The faults and tectonic growth stratigraphy in the southern slope to the Axial Trough in Fig. 6 are interpreted here as due to slope failure. As similar sediments most likely underlie the southerly slope of the Axial Trough (area annotated “Embayment” and “E” in Fig. 1), slope instability may have also occurred there. As mentioned earlier, the mean channel gradient is only $\sim 0.5^\circ$. While retrogressive failure cannot be ruled out as having created the channel morphology, such a gradient would be small for failure in carbonate shelf sediments. McAdoo et al. (2000) evaluated evidence for slope failure in extensive multibeam bathymetry data around the USA. They found slope failure had occurred in areas of $<1^\circ$ seabed gradient, though they occurred in the clay-rich muddy sediments of the Gulf of Mexico and may have been caused or affected by underlying weak halite deposits. Additionally, the regular, straight morphology of the North Hanish Channel does not match the morphologies of failed slope deposits documented by McAdoo et al. (2000), so it is unlikely to have been created simply by slope failure.

However, the embayments to either side of the channel where it enters the trough (Fig. 1) may have been produced by slope instability. Failure in the lower part of the channel

where it enters the Axial Trough may also potentially explain the knickpoint morphology.

5.3 Tectonic Origin

The present-day stability of the area is suggested by GPS measurements, which show little horizontal movement between the Arabian and African coasts on either side of Hanish Sill (McClusky et al. 2003; Reilinger et al. 2015). The on-going separation of the Nubian and Arabian tectonic plates occurs instead to the west of the Danakil Block in the Danakil Depression. How far back in time this limited movement persisted is difficult to assess from plate reconstruction data, though the data also suggest limited movement. Roeser (1975) interpreted seafloor spreading magnetic anomalies along the Red Sea spreading axis to anomaly 3 (4–5 Ma; Cande and Kent 1995) at 16°N , but the anomalies become confused south of $15^\circ30'\text{N}$ and die out entirely south of 15°N (Chu and Gordon 1998), as would be expected if the Danakil Block had continued rotating while effectively joined to Arabia in the south after anomaly 3. The rotation pole for Danakil relative to Arabia of Chu and Gordon (1998) lies to the SE with a 95% error ellipse almost reaching the Bab al Mandab Strait. Plate tectonic reconstructions of the Danakil Block (Eagles et al. 2002) based on the Chu and Gordon (1998) rotation poles show only modest (a few tens of km at most) separation of the southern part of that block relative to Arabia since 5 Ma.

The success in detecting the NNW-trending feature in the Bouguer anomalies (Fig. 7b) suggests that sediment-filled features of a few hundred metres in relief should be observable in the data. The lack of any such feature over the North Hanish Channel suggests that any fault throw if it exists is likely to be only modest ($<100 \text{ m}$). The Bouguer data rather suggest that two tectonic features occur with significant relief, the NNW- and NNE-trending features. Hanish Island and its superimposed cones are also aligned with the latter orientation. Hanish Sill appears to be an isolated block, possibly underlain by denser material, encompassed on its NE and SE sides by faults or fault zones. The sill may have been stable or only gradually moving vertically, as modelling of sedimentary $\delta^{18}\text{O}$ suggests that the sill has been uplifting during the last 500 ky by $\sim 0.02 \text{ m kyr}^{-1}$ (Rohling et al. 2009). This interpretation might be supported if the two trends marked on Fig. 7 are normal faults or transcurrent faults that have had normal components of slip, so that Hanish Sill lies within their footwalls and the faults have been modestly active. Overall, the gravity data do not obviously support a tectonic origin for the north channel.

5.4 Massive Red Sea Inflow Origin

5.4.1 Morphological Evidence

We compare the North Hanish Channel with the buried channel east of the Camarinal Sill that has been suggested to have been excavated by a massive flow during re-flooding of the Mediterranean (Garcia-Castellanos et al. 2009). That channel has a steeper gradient of $\sim 2^\circ$. It has a similar 8-km width to the North Hanish Channel, although the Hanish channel may have originally been wider and has since narrowed by progradation of sediments shed from the shelves, such as is suggested by some dipping stratigraphy in Fig. 5. Unfortunately, the seismic data in Fig. 5 do not reveal many details of the reflections, although arguably reflections beneath the east slope of Hanish Sill are truncated at the seabed, suggesting erosion.

We highlighted the knickpoint (Fig. 4) in our observations section. Steep sections of river bedrock channels and submarine channels form either by strata that are locally resistant to erosion (Miller 1991) or from migration of a steepened gradient because that gradient leads to an intensification of flow and enhanced erosion (Gardner 1983; Mitchell 2006; Seidl and Dietrich 1992). Rapid inflow of Gulf of Aden waters could potentially explain the occurrence of the knickpoint in the North Hanish Channel (Fig. 4). Accordingly, during inflow, the acceleration of the inflowing waters as they entered the Axial Trough could have produced a wave of erosion.

When we describe river or submarine channels as “tectonically controlled”, in practice we mean that fault or fold topography has guided the flows, leading to greater erosion along their paths, or that breccias created by fault movements left the rocks more susceptible to erosion. Although there is no Bouguer anomaly associated with the channel, less significant fault displacement (~ 100 m) is not ruled out by the gravity data and smaller faults aligned with the Axial Trough would explain the straight morphology of the channel in plan view.

5.4.2 Feasibility of Channel Excavation

We cannot accurately know the discharge of any influx without knowing the geometry of any structure that was breached. However, we can say that it would have been larger than the net evaporation loss of the Red Sea in order to re-flood the sea. In the following section, we explore the implications of such a discharge on the shear stresses within a channel 8-km wide and with a gradient of 1% like the modern North Hanish Channel. We calculate the potential shear stresses imposed by such a flow on its bed. Although we do not have geotechnical information on the eroded materials, we can say that the shear stresses are generally

large compared with shear stresses that occur in bedrock rivers in flood, where erosion is known to occur.

The modern net evaporation (evaporation minus precipitation) is about $30000 \text{ m}^3 \text{ s}^{-1}$ (Maillard and Soliman 1986; Sofianos et al. 2002). If the influx occurred following a Pleistocene sea level drawdown, the net evaporation could have been around half this value because sea level lowered below the shelves would have left the sea covering roughly half of its modern surface area. The LGM (and likely other Pleistocene glacial maxima) evaporation rates were probably comparable to present rates because greater wind speed and lowered atmospheric humidity compensated partly for lowered temperature (Biton et al. 2008). If the event occurred as early as the Late Miocene or early Pliocene, evaporation rates are less well known. The Red Sea basin was narrower than it is today because it has widened subsequently with plate tectonic spreading (by about 60 km on average based on a 12 mm yr^{-1} spreading rate in the basin center (Mitchell and Park 2014), or about 20% of the present area). Common occurrences of fluvial clastic deposits in the upper Miocene Zeit Formation suggest that the climate was wetter in the Miocene (Griffin 1999), further suggesting that the evaporative loss was much less than the present-day $30000 \text{ m}^3 \text{ s}^{-1}$.

After accelerating from Hanish Sill onto the channel gradient, the flow would have approached equilibrium. The velocity u (m s^{-1}) of that spillway flow can be estimated using standard hydraulic relationships. Manning’s Formula for depth-averaged flow speed (Webber 1971) suggests at equilibrium:

$$u = \frac{R^{2/3} S^{1/2}}{n} \quad (1)$$

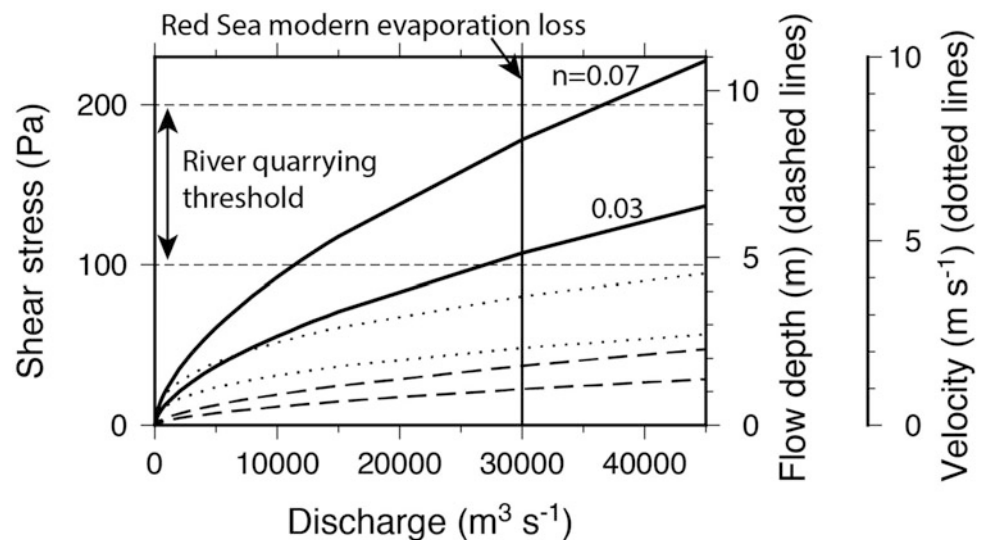
where R is the hydraulic radius (m), S is the dimensionless channel gradient and n is a constant representing friction of the channel boundaries. For the following estimates, values of $n = 0.03$ and 0.07 were used, appropriate for channel roughness corresponding with gravels or boulders (Webber 1971). For wide channels such as the channel here, the hydraulic radius is approximately equal to the flow depth d .

Discharge $Q = uA$, where A is the flow cross-sectional area $A = bd$ and b is the depth-averaged width. Substituting u from Eq. (1) in $Q = ubd$ and rearranging:

$$d = \left(\frac{nQ}{S^{1/2}b} \right)^{3/5} \quad (2)$$

Various properties of a hypothetical spillway flow were computed using these relationships, with the modern spillway average gradient $S = 0.01$ (0.5°) and with discharge Q varied up to $45000 \text{ m}^3 \text{ s}^{-1}$. The shear stress for equilibrium flow shown in Fig. 8 was estimated from flow weight resolved parallel to the bed (i.e., $\rho_w g d S$).

Fig. 8 Bed shear stress and other hydraulic properties of an open channel equilibrium flow of 8 km width, 1% gradient and with varied discharge. Values were calculated separately with Mannings' constant n of 0.03 and 0.07 (in the case of velocity, the lower dotted line was computed with the higher n -value)



The bed shear thresholds for quarrying in Fig. 8 are based on observations of visible movement of bedrock blocks at 100–200 Pa in a river in flood by Snyder et al. (2003). That this threshold might apply more generally to rivers is suggested by compiled flood shear stresses from various tectonic and climatic settings, which have values limited mostly to the range 100–1000 Pa (Mitchell 2014; Mitchell et al. 2012). If the substrate eroded along the channel comprised jointed indurated materials, this threshold could be appropriate. If the materials were less indurated, a lower threshold would be more appropriate.

The graphs in Fig. 8 suggest that inflow discharge at half the modern evaporation loss would produce stresses mostly just below the threshold for bedrock erosion, though probably within the range of erosion of less indurated materials. On the other hand, if the inflow occurred at greater discharge because of abrupt failure of an obstruction, the stresses could have been sufficient to erode bedrock. These calculations are not intended to test the likelihood of an inflow event, though they demonstrate that channel excavation with reasonable discharge values is a viable explanation for the channel.

5.4.3 Paleoceanography

The possibility of a deep drawdown of the Red Sea and subsequent re-flooding is not expected from reading the literature of the Plio-Pleistocene. During the Late Pleistocene glacial stages (to ~ 500 ka, constrained by continuous sediment cores), the sea appears not to have become completely isolated and hypersaline because $\delta^{18}\text{O}$ values in Red Sea pelagic sediments remained comparable with LGM values that represent continuous though restricted exchange with the Gulf of Aden (Biton et al. 2008; Rohling et al. 2009; Siddall et al. 2003, 2004). Furthermore, some benthic foraminifera and pteropods survived through those stages,

suggesting a lack of hypersalinity (Almogi-Labin et al. 1998; Fenton et al. 2000).

In the Miocene, the solutes that formed the Red Sea evaporites were probably supplied by seawater from the Mediterranean (Bosworth et al. 2005; Coleman 1974; Hughes et al. 1992; Orszag-Sperber et al. 1998). Evidence for this includes calcareous nannofossils identified by Boudreaux (1974) within the intercalated black shales of the evaporites drilled at DSDP Sites 225 and 227 in the central Red Sea, which have affinities with the Mediterranean (Orszag-Sperber et al. 1998), and Mediterranean fauna in marginal commercial wells (e.g., Bunter and Abdel Magid 1989; Hughes 2014).

At some uncertain date, a transition occurred between Mediterranean exchange to Indian Ocean exchange with the opening of the Bab el Mandab Strait (Hughes et al. 1992; Orszag-Sperber et al. 1998; Richardson and Arthur 1988) (Fig. 1). By the early Pliocene, an uplifted sill separated the Red Sea from the Mediterranean and an Indian Ocean fauna invaded the Red Sea (Orszag-Sperber et al. 1998; Purser and Hötzel 1988; Swartz and Arden 1960). Seismic reflection data bear on the issue of isolation. Those data from the central Red Sea show a reflective upper Pleistocene, which can be explained by layers of preferentially more rigid, and hence higher seismic velocity, aragonite-rich sediment produced when the sea was more saline during sea-level lowstands (Almogi-Labin et al. 1996; Milliman et al. 1969; Mitchell et al. 2015). In contrast, the lower Plio-Pleistocene is typically more transparent in seismic reflection data from the central and southern Red Sea (summarized by Mitchell et al. 2015). Such transparency would be consistent with a lack of seismic impedance variation over sediment intervals equal to or greater than a quarter of a seismic wavelength (a few metres for these data), implying a lack of extreme density and velocity produced by aragonite layers, and hence

ultimately that the sea was continuously exchanging water with the global oceans (Mitchell et al. 2015, 2017).

According to the literature, the only period in which a rapid inflow event is expected to have occurred was at the end of the evaporite stage at the Miocene-Pliocene boundary. Widespread unconformities have been detected at this stratigraphic level in commercial wells (Bunter and Abdel Magid 1989; Hughes et al. 1992) and are observed in seismic data of the S reflection representing the top of the Miocene (Izzeldin 1987; Mitchell et al. 2017). Although coastal erosion during a rising sea could explain these features (Mitchell et al. 2017), rapid sea currents may also help to explain them.

An origin of the channel at the Miocene-Pliocene boundary would seem to be an extreme interpretation given that the boundary is 5.3 million years old. Nevertheless, the currents are maintaining at least the shallower parts of the channel morphology by preventing some sediment deposition. GPS and plate-reconstruction data indicate that modest tectonic movements have occurred across the sill for the last few million years. As the tectonic and slope failure explanations seem weak or at least equivocal, we suggest this more extreme explanation of rapid inflow at the end of the Miocene is worthy of further consideration. Clearly more data (seismic, coring and in situ oceanographic measurements) are required around the North Hanish Channel and the section where it enters the Axial Trough to test this idea.

6 Conclusions

Current meter measurements show large outflows of $\sim 1 \text{ m s}^{-1}$ over Hanish Sill at present, which are likely maintaining the morphology of the shallower parts of the channel around Hanish Sill. However, currents are anticipated to be much weaker below 200 m within Red Sea Deep Water, which lies below Red Sea Outflow Water at intermediate depths, so the lower channel is not obviously explained by the currents. Evidence for slope failure was found in seismic data of the southern slope of the Axial Trough and may have contributed to the lower channel morphology, although the 0.5° gradient of the channel would be low for slope failure in carbonate shelf sediments. Although the available data do not rule out the existence of faults parallel with the Axial Trough, which may have guided inflows and thus explain the straight morphology of the channel, Bouguer gravity anomalies do not reveal any major graben structure under the North Hanish Channel. Therefore, the channel most likely does not have a tectonic origin. By a process of elimination, therefore, the North Hanish Channel may have formed by a massive inflow event, perhaps as long ago as 5.3 Ma at the end of the Miocene evaporite phase.

Acknowledgements Rose Anne Weissel is thanked for help in locating and scanning the RV *Conrad* data used in this study. All other data besides the current meter records used here were obtained from public sources (<http://www.ngdc.noaa.gov/>, <http://www.geomapapp.org/>, <http://topex.ucsd.edu/>). Andrew Goodwillie clarified the origin of data contributing to the GMRT grid in this area. Eelco Rohling explained why deep drawdown was unlikely to have occurred in the late Pleistocene. We would like to thank the Saudi Geological Survey for organizing the publication of this book on the Red Sea. Thanks also to Graeme Eagles for reviewing an earlier version of this chapter and to the three anonymous reviewers of the present chapter for helpful comments. Figures in this article were created with the “GMT” software system (Wessel and Smith 1991).

References

- Almogi-Labin A, Hemleben C, Meischner D, Erlenkeuser H (1996) Response of Red Sea deep-water agglutinated foraminifera to water-mass changes during the Late Quaternary. *Mar Micropal* 28:283–297
- Almogi-Labin A, Hemleben C, Meischner D (1998) Carbonate preservation and climate changes in the central Red Sea during the last 380 kyr as recorded by pteropods. *Mar Micropal* 33:87–107
- Berger WH, Piper DJW (1972) Planktonic foraminifera: differential settling, dissolution and redeposition. *Limn Oceanogr* 17:275–287
- Berthois L, Le Calvez Y (1960) Etude de la vitesse de chute des coquilles de foraminifères planctoniques dans un fluide comparativement à celle de grains de quartz. *Inst Peches Mar* 24:293–301
- Biton E, Hildor H, Peltier WR (2008) Red Sea during the last glacial maximum: implications for sea level reconstruction. *Paleocean* 23:paper PA1214. <https://doi.org/10.1029/2007pa001431>
- Bosworth W, Huchon P, McClay K (2005) The Red Sea and Gulf of Aden basins. *J African Earth Sci* 43:334–378
- Boudreaux JE (1974) Calcareous nannoplankton ranges, Deep Sea Drilling Project Leg 23. In: Whitmarsh RB, Wesser DE, Ross DA (eds) Initial reports of the Deep Sea Drilling Project. US Government Printing Office, Washington, DC, pp 1073–1090
- Bower AS, Johns WE, Fratantoni DM, Peters H (2005) Equilibration and circulation of Red Sea outflow water in the western Gulf of Aden. *J Phys Ocean* 35:1963–1985
- Bunter MAG, Abdel Magid AEM (1989) The Sudanese Red Sea: 1. New developments in stratigraphy and petroleum-geological evolution. *J Petrol Geol* 12:145–166
- Cande SC, Kent DV (1995) Revised calibration of the geomagnetic polarity timescale for the late Cretaceous and Cenozoic. *J Geophys Res* 100:6093–6095
- Cember RP (1988) On the sources, formation, and circulation of Red Sea deep water. *J Geophys Res* 93:8175–8191
- Chang YS, Özgökmen TM, Peters H, Xu X (2008) Numerical simulation of the Red Sea outflow using HYCOM and comparison with REDSOX observations. *J Phys Ocean* 38:337–358
- Chu D, Gordon RG (1998) Current plate motions across the Red Sea. *Geophys J Int* 135:313–328
- Coleman RG (1974) Geologic background of the Red Sea. In: Whitmarsh RB, Wesser OE, Ross DA (eds) Initial reports of the Deep Sea Drilling Project, vol 23. U.S. Government Printing Office, Washington, DC, pp 813–819
- Eagles G, Gloaguen R, Ebinger C (2002) Kinematics of the Danakil microplate. *Earth Planet Sci Lett* 203:607–620
- Einsele G, Werner F (1972) Sedimentary processes at the entrance Gulf of Aden/Red Sea. In: Seibold E, Closs H (eds) “Meteor” Forschungsergebnisse, Reihe C. Bornträger, Berlin, pp 39–62

- Eriş KK, Ryan WBF, Çağatay MN, Sancar U, Lericolais G, Ménot G, Bard E (2007) The timing and evolution of the post-glacial transgression across the Sea of Marmara shelf south of İstanbul. *Mar Geol* 243:57–76
- Fenton M, Geiselhart S, Rohling EJ, Hemleben C (2000) A planktonic zones in the Red Sea. *Mar Micropal* 40:277–294
- García M, Hernández-Molina FJ, Llave E, Stow DAV, León R, Fernández-Puga MC, Río V, Somoza L (2008) Contourite erosive features caused by the Mediterranean outflow water in the Gulf of Cadiz: quaternary tectonic and oceanographic implications. *Mar Geol* 257:24–40
- García-Castellanos D, Estrada F, Jiménez-Munt I, Gorini C, Fernández M, Vergés J, De Vicente R (2009) Catastrophic flood of the Mediterranean after the Messinian salinity crisis. *Nature* 462:778–782
- Gardner TW (1983) Experimental study of knickpoint migration and longitudinal profile evolution in cohesive homogenous material. *Geol Soc Am Bull* 94:664–672
- Garfunkel Z, Ginzburg A, Searle RC (1987) Fault pattern and mechanism of crustal separation along the axis of the Red Sea from side scan sonar (GLORIA) data. *Ann Geophys* 5B:187–200
- Gass IG (1970) The evolution of volcanism in the junction area of the Red Sea, Gulf of Aden and Ethiopian Rift. *Phil Trans Roy Soc Lond A* 267:369–382
- Griffin DL (1999) The late Miocene climate of northeast Africa: unravelling the signals in the sedimentary succession. *J Geol Soc Lond* 156:817–826
- Hamilton EL, Bachman RT (1982) Sound velocity and related properties of marine sediments. *J Acoust Soc Am* 72:1891–1904
- Hiscott RN, Aksu AE, Yaşar D, Kaminski MA, Mudie PJ, Kostylev VE, MacDonalda JC, İşler FI, Lord AR (2002) Deltas south of the Bosphorus Strait record persistent Black Sea outflow to the Marmara Sea since ~10 ka. *Mar Geol* 190:95–118
- Hughes GW (2014) Micropalaeontology and palaeoenvironments of the Miocene Wadi Waqb carbonate of the northern Saudi Arabian Red Sea. *GeoArabia* 19:59–108
- Hughes GW, Abdine S, Girgis MH (1992) Miocene biofacies development and geological history of the Gulf of Suez. *Egypt. Mar Petrol Geol* 9:2–28
- Ilicak M, Özgökmen TM, Peters H, Baumert HZ, Iskandarani M (2008) Performance of two-equation turbulence closures in three-dimensional simulations of the Red Sea overflow. *Ocean Model* 34:122–139
- Izzeldin AY (1987) Seismic, gravity and magnetic surveys in the central part of the Red Sea: their interpretation and implications for the structure and evolution of the Red Sea. *Tectonophysics* 143:269–306
- Jaroszk E, Murray SP, Inoue M (2005) Observations on the characteristics of tides in the Bab el Mandab Strait. *J Geophys Res* 110:paper C03015. <https://doi.org/10.01029/02004jc002299>
- Lambeck K, Purcell A, Flemming NC, Vita-Finzi C, Alsharekh AM, Bailey GN (2011) Sea level and shoreline reconstructions for the Red Sea: isostatic and tectonic considerations and implications for hominin migration out of Africa. *Quat Sci Rev* 30:3542–3574
- Luján M, Crespo-Blanc A, Comas M (2010) Morphology and structure of the Camarinal Sill from high-resolution bathymetry: evidence of fault zones in the Gibraltar Strait. *Geo-Mar Lett* 31:163–174
- Maillard C, Soliman G (1986) Hydrography of the Red Sea and exchanges with the Indian Ocean in summer. *Oceanol Acta* 9: 249–269
- Manheim FT, Dwight L, Belostock RA (1974) Porosity, density, grain density, and related physical properties of sediments from the Red Sea drill cores. In: Whitmarsh RB, Weser OE, Ross DA (eds) Initial reports of the Deep Sea Drilling Project, vol 23. U.S. Government Printing Office, Washington, DC, pp 887–907
- McAdoo BG, Pratson LF, Orange DL (2000) Submarine landslide geomorphology, US continental slope. *Mar Geol* 169:103–136
- McClusky S, Reilinger R, Mahmoud S, Ben Sari D, Tealeb A (2003) GPS constraints on Africa (Nubia) and Arabia plate motions. *Geophys J Int* 155:126–138
- Miller JR (1991) The influence of bedrock geology on knickpoint development and channel-bed degradation along downcutting streams in south-central Indiana. *J Geol* 99:591–605
- Miller MC, Komar PD (1977) The development of sediment threshold curves for unusual environments (Mars) and for inadequately studied materials (foram sands). *Sedimentology* 24:709–721
- Miller MC, McCave IN, Komar PD (1977) Threshold of sediment motion under unidirectional currents. *Sedimentology* 24:507–528
- Milliman JD, Ross DA, Ku T-L (1969) Precipitation and lithification of deep-sea carbonates in the Red Sea. *J Sed Petrol* 39:724–736
- Mitchell NC (2006) Morphologies of knickpoints in submarine canyons. *Geol Soc Am Bull* 118:589–605
- Mitchell NC (2014) Bedrock erosion by sedimentary flows in submarine canyons. *Geosphere* 10. <https://doi.org/10.1130/ges01008.01001>
- Mitchell NC (2015) Lineaments in gravity data of the Red Sea. In: Rasul NMA, Stewart ICF (eds) *The Red Sea: the formation, morphology, oceanography and environment of a young ocean basin*. Springer Earth System Sciences, Berlin, pp 123–133
- Mitchell NC, Park Y (2014) Nature of crust in the central Red Sea. *Tectonophysics* 628:123–139
- Mitchell NC, Huthnance JM, Schmitt T, Todd B (2012) Threshold of erosion of submarine bedrock landscapes by tidal currents. *Earth Surf Proc Landf* 38:627–639
- Mitchell NC, Ligi M, Rohling EJ (2015) Red Sea isolation history suggested by Plio-Pleistocene seismic reflection sequences. *Earth Planet Sci Lett* 430:387–397
- Mitchell NC, Ligi M, Feldens P, Hübscher C (2017) Deformation of a young salt giant: Regional topography of the Red Sea Miocene evaporites. *Basin Res* 29:352–369
- Neumann AC, McGill DA (1962) Circulation of the Red Sea in early summer. *Deep Sea Res* 8:223–235
- Orszag-Sperber F, Harwood G, Kendall A, Purser BH (1998) Review of the evaporites of the Red Sea-Gulf of Suez rift. In: Purser BH, Bosence DWJ (eds) *Sedimentation and tectonics of rift basins: Red Sea-Gulf of Aden*. Chapman & Hall, London, pp 409–426
- Paphitis D, Collins MB, Nash LA, Wallbridge S (2002) Settling velocities and entrainment thresholds of biogenic sands (shell fragments) under unidirectional flow. *Sedimentology* 49:211–225
- Parsons DR, Peakall J, Aksu AE, Flood RD, Hiscott RN, Besiktepe S, Moulard D (2010) Gravity-driven flow in a submarine channel bend: direct field evidence of helical flow reversal. *Geology* 38:1063–1066
- Peters H, Johns WE (2006) Bottom layer turbulence in the Red Sea outflow plume. *J Phys Ocean* 36:1764–1785
- Pratt LJ, Johns W, Murray SP, Katsumata K (1999) Hydraulic interpretation of direct velocity measurements in the Bab el Mandab. *J Phys Ocean* 29:2769–2784
- Purser BH, Hötzl H (1988) The sedimentary evolution of the Red Sea rift: A comparison of the northwest (Egyptian) and northeast (Saudi Arabian) margins. *Tectonophysics* 153:193–208
- Reilinger R, McClusky S, ArRajehi A (2015) Geodetic constraints on the geodynamic evolution of the Red Sea. In: Rasul NMA, Stewart ICF (eds) *The Red Sea: the formation, morphology, oceanography and environment of a young ocean basin*. Springer Earth System Sciences, Berlin, pp 135–150
- Richardson M, Arthur MA (1988) The Gulf of Suez—northern Red Sea Neogene rift: a quantitative basin analysis. *Mar Petrol Geol* 5:247–270
- Roeser HA (1975) A detailed magnetic survey of the southern Red Sea. *Geol Jahrb* 13:131–153
- Rohling EJ, Grant K, Bolshaw M, Roberts AP, Siddall M, Hemleben C, Kucera M (2009) Antarctic temperature and global sea level closely coupled over the past five glacial cycles. *Nature Geosci* 2:500–504

- Rubin AM (1992) Dike-induced faulting and graben subsidence in volcanic rift zones. *J Geophys Res* 97:1839–1858
- Ryan WBF, Carbotte SM, Coplan JO, O'Hara S, Melkonian A, Arko R, Wiessel RA, Ferrini V, Goodwillie A, Nitsche F, Bonczkowski J, Zemsky R (2009) Global multi-resolution topography synthesis. *Geochem Geophys Geosys* 10:Paper Q03014
- Sandwell DT, Smith WHF (1997) Marine gravity anomaly from Geosat and ERS-1 satellite altimetry. *J Geophys Res* 102:10039–10054
- Sandwell D, Müller RD, Smith WHF, Garcia E, Francis R (2014) New global marine gravity model from CryoSat-2 and Jason-1 reveals buried tectonic structure. *Science* 346:65–67
- Seidl M, Dietrich WE (1992) The problem of channel erosion into bedrock. In: Schmidt KH, de Ploey J (eds) *Functional geomorphology: landform analysis and models*. Catena Supplement, vol 23, pp 101–124
- Siddall M, Rohling EJ, Almogi-Labin A, Hemleben C, Meischner D, Schmeizer I, Smeed DA (2003) Sea-level fluctuations during the last glacial cycle. *Nature* 423:853–858
- Siddall M, Smeed DA, Hemleben C, Rohling EJ, Schmeizer I, Peltier WR (2004) Understanding the Red Sea response to sea level. *Earth Planet Sci Lett* 225:421–434
- Smeed DA (2004) Exchange through the Bab el Mandab. *Deep-Sea Res II* 51:455–474
- Smith WHF, Sandwell DT (1997) Global sea floor topography from satellite altimetry and ship soundings. *Science* 277:1956–1962
- Smith WHF, Wessel P (1990) Gridding with continuous curvature splines in tension. *Geophysics* 55(3):293–305
- Snyder NP, Whipple KX, Tucker GE, Merritts DJ (2003) Importance of stochastic distribution of floods and erosion thresholds in the bedrock river incision problem. *J Geophys Res* 108:ETG 17-11–ETG 17-15. <https://doi.org/10.1029/2001jb001655>
- Sofianos SS, Johns EW (2003) An oceanic general circulation model (OGCM) investigation of the Red Sea circulation, 2. Three-dimensional circulation in the Red Sea. *J Geophys Res* 107:Paper 3066. <https://doi.org/10.1029/2001jc001185>
- Sofianos SS, Johns EW (2007) Observations of the summer Red Sea circulation. *J Geophys Res* 112:Paper C06025. <https://doi.org/10.1029/2006jc003886>
- Sofianos SS, Johns EW, Murray SP (2002) Heat and freshwater budgets in the Red Sea from direct observations at Bab el Mandeb. *Deep-Sea Res II* 49:1323–1340
- Southard JB, Young RA, Hollister CD (1971) Experimental erosion of calcareous ooze. *J Geophys Res* 76:5903–5909
- Swartz DH, Arden DD (1960) Geologic history of the Red Sea area. *Bull Am Assoc Petrol Geol* 44:1621–1637
- Telford WM, Geldart LP, Sheriff RE, Keys DA (1976) *Applied geophysics*. Cambridge University Press, New York, p 860
- Webber NB (1971) *Fluid mechanics for civil engineers*. Chapman and Hall, New York, p 340
- Werner G, Lange K (1975) A bathymetric survey of the sill area between the Red Sea and the Gulf of Aden. *Geologisches Jahrbuch D* 13:125–130
- Wessel P, Smith WHF (1991) Free software helps map and display data. *EOS Trans Am Geophys Union* 72:441
- Whitmarsh RB, Weser OE, Ross DA (1974) *Initial reports of the Deep Sea Drilling Project, 23B*. U. S. Government Printing Office, Washington, DC